Soft Matter

PAPER

View Article Online
View Journal | View Issue

Cite this: *Soft Matter*, 2026, **22**, 763

Microbubble-based measurement of shear and loss moduli in polyacrylamide hydrogels at MHz frequencies

Ali Rezaei, [a] Kay Dijs, [a] David Fernandez Rivas, [b] Jacco H. Snoeijer, [a] Michel Versluis [a] and Guillaume Lajoinie*[a]

The rheology of soft materials is routinely measured at low strain rates to extract constitutive laws necessary for understanding and modeling their behavior. High-frequency rheology, however, remains difficult to access. Consequently, the mechanical properties of soft materials at MHz strain rates are largely unknown. Ultrasound-driven microbubbles, widely used in biomedical imaging, drug delivery, and therapy, act as efficient mechanical actuators at MHz frequencies. Their dynamics depend on nonlinear resonance behavior, the viscoelasticity of their stabilizing shells, and the viscoelastic properties of the surrounding medium. Here, we make use of (nonlinear) bubble dynamics to characterize the rheology of polyacrylamide (PAM) hydrogels at strain rates exceeding 10^6 s^{-1}. Narrow resonance curves of single coated microbubbles embedded in PAM, obtained through high-speed imaging, were compared to a Rayleighâ€"Plesset-type model. The results show that the shear modulus is similar in both the Hz and MHz regimes, while the loss modulus behaves very differently, exhibiting an effective shear viscosity at MHz frequencies comparable to that of water. These findings demonstrate a new approach for probing the high-frequency rheology of viscoelastic media.

Received 26th May 2025,
Accepted 13th December 2025

DOI: 10.1039/d5sm00552c

rsc.li/soft-matter-journal

1 Introduction

Ultrasound contrast agents (UCAs) are widely used in medical imaging to enhance contrast and improve medical diagnosis, *e.g.*, for organ perfusion imaging or to monitor hypervascularization in and around tumors.[1,2] Additionally, UCAs are intensively investigated for their ultrasound-mediated therapeutic potential. Microbubbles can indeed increase the permeation of endothelial layers, resulting in the local delivery of drugs or genes.[3,4]

Ultrasound contrast microbubbles have a typical size in the range of 1 to 5 μm in radius. They are filled with a low-solubility high-molecular weight gas, such as sulfur hexafluoride (SF_6), or a perfluorocarbon (C_3F_8, or C_4F_{10}), and are stabilized by a shell (most often consisting of a phospholipid mixture) that reduces the interfacial pressure of the microbubbles and hinders the diffusion of gas from the bubble core into the surrounding medium,[5–7] which otherwise leads to rapid bubble dissolution.

Upon exposure to ultrasound, microbubbles undergo (nonlinear) volumetric oscillations which are key to their superior scattering cross-section. Furthermore, when the driving frequency is tuned to the resonance frequency of the bubbles, they experience a mechanical resonance with larger bubble oscillations and higher scattering, as well as the generation of nonlinear harmonics, that thus further enhances contrast generation. This unique behavior is routinely exploited in clinical imaging, both in linear and nonlinear contrast imaging modes.

The ultrasound-driven response of UCAs, including the effects of the phospholipid coating, is very well understood in infinitely large media, *i.e.*, where the bubble is free from interactions with boundaries or neighboring bubbles. These dynamics have been measured through both acoustic attenuation and high-speed imaging experiments[8–10] and are well described by Rayleigh–Plesset-type models.[7] In many biomedical applications such as perfusion imaging, ultrasound localization microscopy, targeted imaging, drug delivery, and blood-brain-barrier opening, bubbles are not oscillating in field. There, the presence of neighboring viscoelastic tissue has a crucial effect on their dynamics. This includes both their linear resonance behavior and their nonlinear dynamics.[11] For example, phagocytosed microbubble were shown to have a different behavior than free bubbles.[12] Furthermore, the presence of a viscoelastic boundary (*e.g.*, a vessel wall) can increase[13–15] or

[a] *Physics of Fluids Department, Faculty Science and Technology, University of Twente, P.O. Box 217, Enschede, 7500AE, The Netherlands. E-mail: g.p.r.lajoinie@utwente.nl*
[b] *Mesoscale Chemical Systems (MCS), Faculty Science and Technology, University of Twente, P.O. Box 217, Enschede, 7500AE, The Netherlands*

decrease[13] the bubbles' resonance frequency depending on the elasticity of the material, and that confinement decreases the bubbles' oscillation amplitude.[14,16] In the bulk of a viscoelastic medium, it has been shown that elasticity of the medium can increase the resonance frequency of bubbles, while the additional viscous dissipation can lead to overdamped dynamics.[17,18]

Directly investigating bubble oscillations in tissues in a controlled way is challenging, owing to the opacity, complexity, and variability within and across soft tissues. A first step can therefore comprise a study of the oscillations of ultrasound contrast microbubbles in much simpler materials. While this does not offer a direct translation toward real tissue, it allows to better understand meaningful fundamental aspects. For example, the oscillations of microbubbles in tissues have previously been modeled by adding a linear Kelvin–Voigt (K–V) viscoelastic model or a nonlinear Neo-Hookean elastic model to a Rayleigh–Plesset-type equation.[19] Originally, Allen and Roy have developed a framework to compute the oscillations of bubbles in arbitrary linear[20] and nonlinear[21] viscoelastic media by solving the bubble dynamics equation in conjunction with a stress tensor analysis. This approach was extended by Stride *et al.* to model the oscillations of bubbles in blood, including both a linear viscoelastic shell and a linear viscoelastic effect of the red blood cells.[22] More recently, Oratis *et al.*[23] have developed a unifying framework that allows for a straightforward numerical integration based on the relaxation function of linear viscoelastic media. One major issue that remains is that the use of any of these models requires *a priori* knowledge of the viscoelastic properties of tissue, which is generally not the case. More specifically, it is well known that the response of a viscoelastic material strongly depends on shear rate.[24,25] However, classical rheology measurements can reach a shear rate up to 10^2 s^{-1}, which is 3 orders of magnitude lower than typical ultrasound driving frequencies.[24]

Earlier experimental studies have employed a range of methods to investigate the rheology of viscoelastic materials at high strain rates.[26,27] Bertin *et al.*[28] utilized atomic force microscopy to study the rheological properties of a medium by observing the displacement of a particle at strain rates of hundreds s^{-1}. Jamburidze *et al.*[17] measured the elastic moduli at a strain rate of 10^4 s^{-1} by fitting the linear oscillation amplitude and resonance frequency of 150 μm bubbles to the resonance curves extracted from high-speed recordings. A very similar experiment was performed later by Murakami *et al.*,[29] with bubbles of similar size, but generated using a laser. These studies have offered deeper insights into medium rheology by pushing farther the boundary of measurable elastic moduli in terms of strain rates. Acoustic methods, such has shear wave elastography,[30] acoustic radiation force impulse imaging (or ARFI),[31] acoustic particle palpation[32] have also been used to characterize tissues in the (sub-)kHz range, and some even found their way to the clinics. However, these methods do not reach strain rates of 10^6 s^{-1},[27,33] which are relevant for biomedical ultrasound. Interestingly, Estrada *et al.*[24] have proposed that a strain rate of 10^8 s^{-1} can be achieved by inertial collapse. This, however, is not an oscillatory method and does not directly provide G' and/or G''. Rheological measurement can be pushed to higher strain rates through the use of smaller microbubbles contained in the medium while being driven by ultrasound. However, such small microbubbles must be stabilized by a shell and the measured response is thus a combination of (known) shell rheology and medium rheology.

In this article, we combine stabilized microbubbles known from the field of ultrasound contrast imaging and optically clear hydrogels with a tunable elasticity to investigate the feasibility of MHz-range rheology using microbubbles. To that end, we use ultra-high-speed imaging of phospholipid-coated microbubbles to extract the shear moduli of a polyacrylamide hydrogel in the 10^6 s^{-1} range. Exploiting the narrowband resonance of microbubbles, we can use Rayleigh–Plesset type equation modified by a linear Kelvin–Voigt viscoelastic model to extract the local (in terms of strain rates) storage and loss moduli of the viscoelastic material in the range of 10^6 to 10^7 s^{-1}.

2 Bubble dynamics model

The Rayleigh–Plesset (RP) equation of motion for a spherically symmetric gas bubble in an incompressible and uniform medium, in the linear regime of deformation of a viscoelastic medium (traceless stress tensor) can be expressed as follows:[20,34]

$$\rho_m\left(R\ddot{R}+\frac{3}{2}\dot{R}^2\right)=P_g(R)-P_\infty-\frac{2\sigma}{R}+3\int_R^\infty\frac{\tau_{rr}}{r}dr. \quad (1)$$

Here, R represents the radius of the bubble, and $\dot{R}$ and $\ddot{R}$ are the first and second derivatives of R with respect to time, respectively. ρ_m is the density of the medium and $P_g(R)$ is the pressure inside the bubble, and P_∞ is the pressure in the liquid far away from the bubble. σ represents the surface tension at the gas–liquid interface while τ_{rr} represents the radial normal stress component, and r is the radial distance from the center of the bubble.[11,35,36]

The modeled system is represented in Fig. 1a. The pressure in the bubble, $P_g(R)$, can be expressed using a polytropic law:[37]

$$P_g(R)=\left(P_0+\frac{2\sigma}{R_0}\right)\left(\frac{R_0}{R}\right)^{3\gamma}. \quad (2)$$

Here, γ is the polytropic exponent of the gas. The vapor pressure is neglected as it is only a small fraction ($\sim$2%) of the total gas pressure. The bubbles considered are small compared to the ultrasound wavelength. Therefore, the pressure in the medium far from the bubble wall P_∞, is the sum of the atmospheric pressure P_0 and of the acoustic driving pressure, P_{ac}. The effect of the phospholipid coating is taken into account by adding a size-dependent surface tension $\sigma(R)$. We describe the elasticity of the shell with the Marmottant model.[38] This model, albeit simple, was experimentally validated.[39] In the dissipation term $(4\kappa_s\dot{R}/R^2)$ where κ_s is the dilatational viscosity of the shell.[39]

For an incompressible, homogeneous, and isotropic linear viscoelastic medium (in the small deformation regime), the Kelvin–Voigt model gives the relation: $\tau_{rr} = 2(G\varepsilon_{rr} + \mu\dot{\varepsilon}_{rr})$. Here,

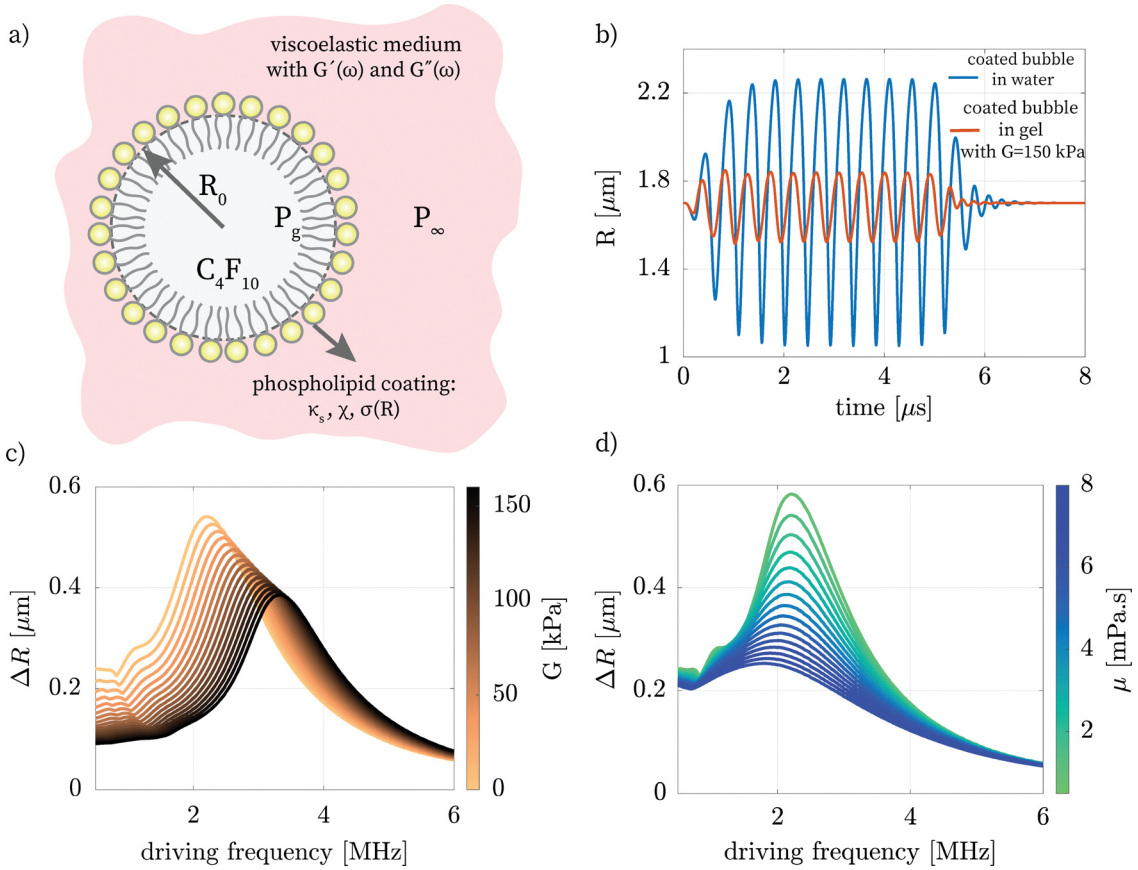

Fig. 1 (a) Schematic and relevant parameters for a phospholipid-coated microbubble in a viscoelastic medium. (b) Radial response for a coated bubble in water (μ = 1 mPa s) and in a viscoelastic medium (G = 150 kPa and μ = 1 mPa s). (c) Resonance curves of a coated microbubble in media with a viscosity of μ = 1 mPa s and G ranging from 0 to 150 kPa. (d) Resonance curves of a coated microbubble for media with G = 0 Pa and μ ranging from 1 to 8 mPa s.

G represents the shear modulus and $\varepsilon_{rr} = -2(R^3 - {R_0}^3)/3r^3$ is the shear strain. μ and $\dot{\varepsilon}_{rr} = -2R^2\dot{R}/r^3$ are the shear viscosity and strain rates, respectively.[40] Substituting τ_{rr} in eqn (1) leads to ref. 11:

$$\rho_m\left(R\ddot{R} + \frac{3}{2}\dot{R}^2\right) = \left(P_0 + \frac{2\sigma(R_0)}{R_0}\right)\left(\frac{R_0}{R}\right)^{3\gamma} - P_0 - P_{ac} - \frac{2\sigma(R)}{R} - \frac{4\kappa_s\dot{R}}{R^2} - \frac{4\mu\dot{R}}{R} - \frac{4G}{3}\left(\frac{R^3 - {R_0}^3}{R^3}\right). \quad (3)$$

Note that a linear model was used to construct a term that appears to be nonlinear ($\sim 1/R^3$). This term is thus only valid if the small deformation condition is met, in other words, this model should only be used in the linear elastic regime of the medium.[19,23]

The specific choice of a Kelvin–Voigt model may seem arbitrary. However, in the limit of a linearized model *i.e.* a first-order viscoelastic description, the contribution of the viscoelastic medium will always add two linear damping and elastic contributions, that are both represented in eqn (3). Although the Kelvin–Voigt model may not be valid at all time-scales (strain rates), it can be used to describe any arbitrary (linear) medium in an infinitesimal frequency band. This is the strength of the approach, which remains valid as long the storage and loss moduli do not significantly vary over the bandwidth of the bubble resonance used to measure them.

The complex modulus is defined as $G^*(\omega) = G'(\omega) + iG''(\omega)$ and describes the entire viscoelastic behavior of the material. $G'(\omega)$ is the storage modulus which represents the solid-like (elastic) response of the material, $G''(\omega)$ is the loss modulus which represents liquid-like (viscous) properties of the material and ω is the angular frequency (strain rate). In the Kelvin–Voigt model, $G = G'$ and $G'' = \mu\omega$.[41]

In the linear bubble oscillation regime eqn (3) can be linearized, which leads to an expression for the eigenfrequency of the bubble:[7]

$$f_0 = \frac{\omega_0}{2\pi} = \frac{1}{2\pi R_0}\sqrt{\frac{1}{\rho_m}\left(3\gamma P_0 + (3\gamma - 1)\frac{2\sigma(R_0)}{R_0} + \frac{4\chi_{eff}}{R_0} + 4G\right)}, \quad (4)$$

with $\sigma(R_0)$ the surface tension of the bubble at rest and χ_{eff} the effective surface elasticity of the shell.[9] This effective elasticity is finite for infinitesimally small oscillations, and gradually decreases for larger amplitudes of oscillation. For reference, the shell elasticity has a minor impact on the resonance frequency for amplitudes of oscillations above approximately 25% of the

resting radius, but must still be considered to accurately extract the viscoelastic parameters of the medium. Linearizing eqn (3) also provides an expression for the damping, which includes viscous dissipation at the interface and shell dissipation, which is dominant over the other damping terms, *i.e.* acoustic reradiation and thermal damping.[42,43]

As an illustration of the effect of viscoelasticity, Fig. 1b compares the solution of eqn (3) for a coated bubble in water to that in a hydrogel with a modulus of 150 kPa, which is the upper range that can be expected for soft tissue, at low strain rates.[44,45] The bubble with R_0 = 1.7 μm is driven at a frequency of 2.2 MHz (its resonance frequency in water) with a 15-cycle, 10-kPa ultrasound pulse tapered with a 2-cycle hyperbolic tangent (tanh) envelope. Increasing the medium's elasticity leads to a decrease in bubble excursion. This is due to the increased medium stiffness, both directly by offering more mechanical resistance to bubble expansion (a lower gain of the system), and indirectly by shifting the bubble's resonance frequency as compared to that in water.[19] The resonance curves obtained by numerical integration of eqn (3) are further presented in Fig. 1c and d for a varying shear modulus and viscosity, respectively, at an acoustic driving pressure of 100 kPa. They show the independent effect of the elastic modulus, affecting the resonance frequency, and of the viscosity, affecting the damping of the system, in the context of the Kelvin–Voigt model.

3 Materials and methods

3.1 Experimental procedure

3.1.1 Microbubble production. Phospholipid-coated microbubbles were produced using a microfluidic platform built in-house.[46] The machine contains a flow-focusing chip to generate highly reproducible mono-sized microbubbles. In the chip, a gas inflow is focused through a narrow orifice using two orthogonal liquid flows containing phospholipids, which generates bubbles through hydrodynamic instability.[47] The phospholipid formulation contained a 9 : 1 molar ratio of DSPC and DPPE–PEG 5000, with a concentration of 12.5 mg mL^{-1} in Isoton (Beckman Coulter, ISOTON II Diluent). The bubbles were filled with a gas mixture of 15 v% of C_4F_{10} gas in CO_2 as detailed by Segers *et al.*[48] Bubble production rate were on the order of one million bubbles per second. Two bubble populations were produced with mean radii of 1.7 and 2.3 μm, and with a polydispersity index on the order of 5%.[46]

3.1.2 Viscoelastic phantom preparations. The phospholipid-coated microbubbles were embedded in polyacrylamide (PAM) hydrogels. These hydrogels are commonly used for their viscoelastic properties that resemble those of soft tissues, at low strain rates.[49,50] In addition, PAM presents multiple advantages. First, they have excellent optical transparency, which makes them suitable for optical characterization, *e.g.*, through ultra-high-speed imaging. Second, their similarity to tissue extends to their acoustic properties, which makes the acoustic excitation of microbubbles straightforward with standard immersion transducers. Finally, their rheological properties can be tuned by adjusting the acrylamide concentration which allows to vary the stiffness of the hydrogel.

Table 1 Formulation for the preparation of the polyacrylamide hydrogel

Materials	Soft hydrogel (6.4% PAM)	Stiff hydrogel (16% PAM)
40% acrylamide (mL)	1.6	4
APS (mg)	14	14
TEMED (μL)	4	4
MilliQ water (mL)	8.4	6

Samples are prepared using the recipe outlined in Table 1.[50] When the monomer acrylamide (Acrylamide/bis 19 : 1, 40 w/v%, SERVA) undergoes polymerization with APS (Ammonium Persulfate, ACS reagent ≥ 98.0%, Sigma-Aldrich), the polymer forms a cross-linked network, which increases the stiffness of the hydrogel. Microbubbles are added to the acrylamide solution before curing. The rise of the microbubbles to the surface due to buoyancy is prevented by stirring the solution until solidification begins. TEMED (*N*,*N*,*N*′,*N*′-tetramethylethylenediamine, ReagentPlus, 99%) is added as a catalyst to speed up the reaction. Since the polymerization is exothermic, the concentration of TEMED was reduced as compared to standard recipes. In combination with a cold bath, this allows to keep the temperature below 35 °C so as not to damage the coated microbubbles. The native acrylamide/bis solution was diluted with MilliQ water to create 6.4% and 16% PAM hydrogels, referred to as the soft and stiff hydrogels, respectively.

The mechanical properties of these hydrogels at low strain rates ($<16\ s^{-1}$) were evaluated using a rotational rheometer (MCR 502e, Anton-Paar) set-up in a parallel plate configuration. To ensure proper contact between the hydrogel and the platform, the samples were cured directly on the rheometer platform. The top parallel plate was lowered to form a gap of 0.5 mm. After curing, a frequency sweep test was performed with 5% strain to measure the storage and loss moduli.

3.1.3 Ultra-high-speed imaging experiments. The dynamics of acoustically-driven phospholipid-coated microbubbles in soft and stiff PAM hydrogels were captured using ultra-high-speed imaging (Shimadzu HPV-X2) at a frame rate of 10 million frames per second, see Fig. 2. A 12-cycle ultrasound pulse, tapered with a 2-cycle tanh envelop was transmitted from a single-element immersion transducer (center frequency 2.25 MHz, C305 SU, Olympus) driven by a programmable arbitrary waveform generator (8026, Tabor Electronics Ltd) connected to a high-power RF amplifier (VBA100–200, Vectawave). Prior to recording the bubble response, we verified that no other bubble is present in the vicinity (several hundred microns) of the target bubble to avoid acoustic cross talk. The transducer was calibrated using an optical fiber hydrophone (Precision Acoustics, UK) to maintain a constant pressure at the focus for each transmit frequency.[51] Fig. 2a shows the experimental setup and Fig. 2b shows snapshots of a typical high-speed recording.

The radius-time curves of oscillating microbubbles in the hydrogel were obtained by analyzing the high-speed recordings

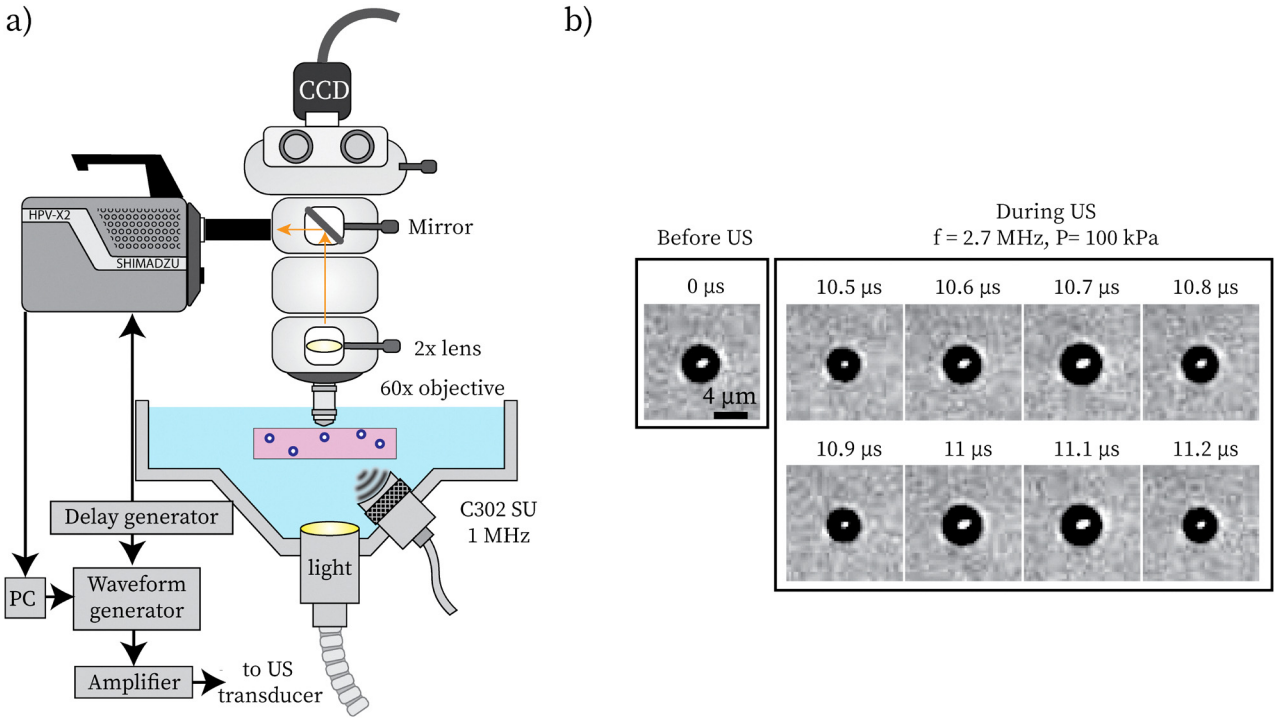

Fig. 2 (a) Schematic of the experimental setup. (b) Snapshots of an ultra-high-speed recording of an oscillating microbubble with an initial radius of R_0 = 1.7 µm in a soft hydrogel with a shear modulus of $G(\omega \to 0) \approx 70$ kPa. The interframe time is 100 ns.

with a custom edge detection MATLAB script.[51] The frequency content of the microbubble oscillations was determined by performing a fast Fourier transform (FFT) on the radius-time curves in MATLAB. No measurable non-spherical effects or shape modes were observed in our optical recordings. The initial bubble radius found in each movie was determined as the median radius over the first 5 frames prior to ultrasound exposure, and the bubble radius that was retained is the median of these individual radii.

3.2 Numerical methods

Fitting eqn (3) to the experimental data requires a minimum of 3 fitting parameters: G, μ, and P_{ac}. The former two are the sought-after quantities. The latter is a non-negligible experimental uncertainty. The local driving pressure P_{ac} is indeed not known precisely in the hydrogel. This is due, first, to the calibration of the needle hydrophone which are accurate within 20%, and second, due to transmission into the hydrogel (at an incidence angle of $\sim 45^\circ$ and refraction).

The experimental data was fitted to eqn (3) using the nonlinear optimization routine lsqnonlin in Matlab in 4 steps. The first step allows to find a coarse estimate of the global minimum by smoothing the data with a shape-preserving spline (see Fig. 3c), and fitting the linearized version of eqn (3) for small relative oscillation amplitude $x \ll 1$:

$$\left|\frac{x}{P_{ac}}\right| = \frac{\frac{1}{\rho_m R_0^2}}{\sqrt{(\omega_0^2 - \omega^2)^2 + (2\zeta\omega\omega_0)^2}}, \quad (5)$$

with ζ the total damping ratio. The ultrasound pulse, for all fitting steps, consisted of a 15-cycle ultrasound pulse, tapered with a 2-cycle tanh envelop, to match the experiments. The amplitude from the radius *versus* time curves was extracted using the fast Fourier transform, in an identical fashion as for the experimental data. Fitting the data to the linearized equation eqn (5) requires an estimate of the effective shell stiffness χ_{eff}. Since χ_{eff} mostly depends on the amplitude of oscillation of the microbubble, it was estimated numerically solving eqn (3) for the bubble size measured in the experiments, and for G = 0 kPa. In the second step, the parameters predicted in the first step were used as initial guess to fit the unfiltered experimental resonance curve to eqn (5). The outcome of this fit is referred to as the "linear fit". The third step uses the parameters predicted in step 2 as initial guess to fit eqn (3) to the data smoothed with a shape-preserving spline. This allows for finding the global minimum for the nonlinear equation. In step 4, the operation was repeated on the unfiltered data. The outcome is referred to as the "nonlinear fit".

In all cases, the residual was defined as the experimental resonance curve, *i.e.*, bubble oscillation amplitude *versus* ultrasound transmit frequency, minus the computed resonance curve. Since (i) the method is narrow-band by design and (ii) the transducer output tends to be distorted at the edge of its bandwidth, the residual was weighted by an envelope that was constructed based on the frequency range used in the measurement:

$$\mathrm{env}(f) = \frac{\cos(2\pi(f - f_c)/\Delta f) + 1}{2}, \quad (6)$$

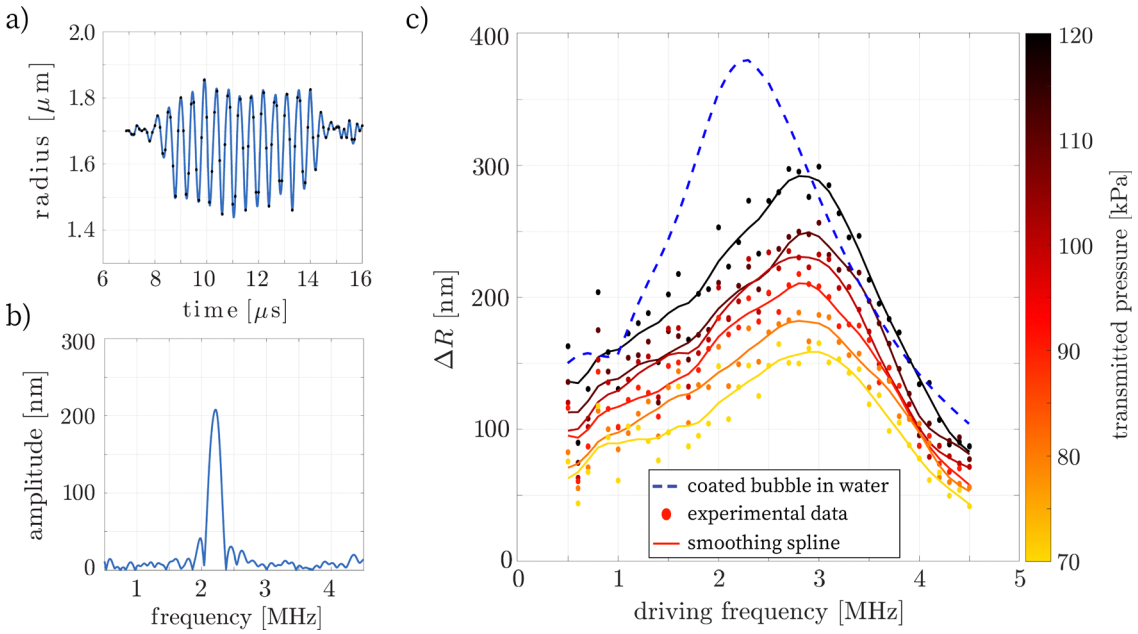

Fig. 3 (a) Bubble radius *versus* time curve, extracted from a high-speed recording. The bubble was driven at a frequency of 2.2 MHz and at a pressure of 100 kPa. Panel (b) shows the Fast Fourier Transform of the data presented in (a). (c) Experimental resonance curve obtained from 41 high-speed recordings for each transmitted acoustic pressure. The pressure ranges from 70 to 120 kPa in steps of 10 kPa. The solid lines are the experimental resonances curves smoothed using a shape-preserving spline. The blue dotted line represents the simulated resonance curve for the same bubble in water for an acoustic pressure P_{ac} = 100 kPa.

where Δf is the frequency range (4 MHz here) and $f_c \approx$ 2.9 MHz is the frequency of maximum response of the bubble, determined from the resonance curves. An example of an experimental resonance curve, smoothed resonance curve, linear fit, and nonlinear fit is shown in Fig. 4.

The 95% confidence intervals of the fitted parameters were determined using the Jacobian returned by lsqnonlin, and the function nlparci. These confidence intervals are given as error bars in Fig. 5.

The effect of the uncertainty caused by an error in determining R_0 was assessed by repeating the fitting procedure with radii lower or higher that the measured radius by ±5 and ±10%.

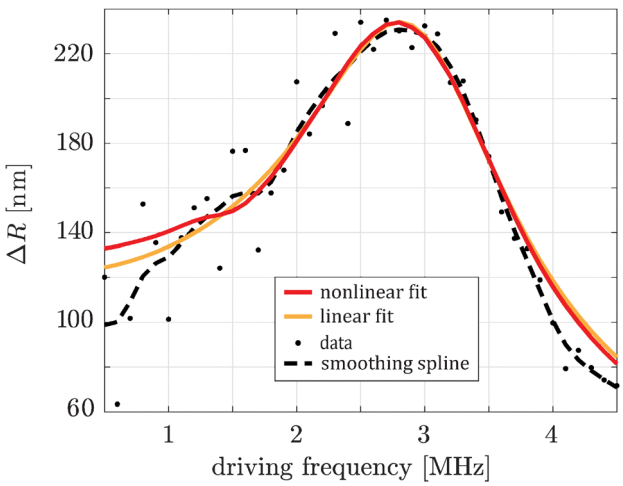

Fig. 4 Example of a fitted resonance curve for P_{ac} = 100 kPa.

Note that the radii extracted from the optical measurements match the size measured using the Coulter Counter and that the size distribution has a polydispersity index (PDI) of 5%.

The other parameters needed to solve eqn (3) and (5) are: $P_0 = 10^5$ Pa, $\rho_m = 10^3$ kg m^{-3}, γ = 1.07 for C_4F_{10} and $\sigma(R \gg R_0)$ = 72 mN m^{-1}. The shell parameters for our typical microbubbles are $\kappa_s = 6 \times 10^{-9}$ kg s^{-1}, χ = 0.5 N m^{-1} and $\sigma(R_0)$ = 0 mN m^{-1}.

4 Results

Fig. 3a shows a typical $R(t)$ curve recorded for a frequency of 2.2 MHz and a pressure of 100 kPa in the soft hydrogel. The black dots are the recorded frames and the solid blue line is a spline interpolation for visualization. The corresponding frequency spectrum is shown in Fig. 3b.

The resonance curves recorded for transmitted pressures ranging from 70 to 120 kPa in steps of 10 kPa are plotted in Fig. 3c. Each curve is constructed from 41 individual recordings of the very same bubble at different driving frequencies. Fig. 3c shows both the recorded data points, and a shape-preserving spline smoothing for visualization, which shows clearly the main features of the resonance curves, and the pressure dependency. A calculated resonance curve for a 1.7 μm coated bubble in water is also shown by the dashed blue line. As compared to water, the presence of the hydrogel increases the resonance frequency of the bubble by about 26% and decreases the radial excursion amplitude by about 47%. Note that, although an amplitude of oscillation on the order of 0.25 times the resting radius may seem large for the regime of linear

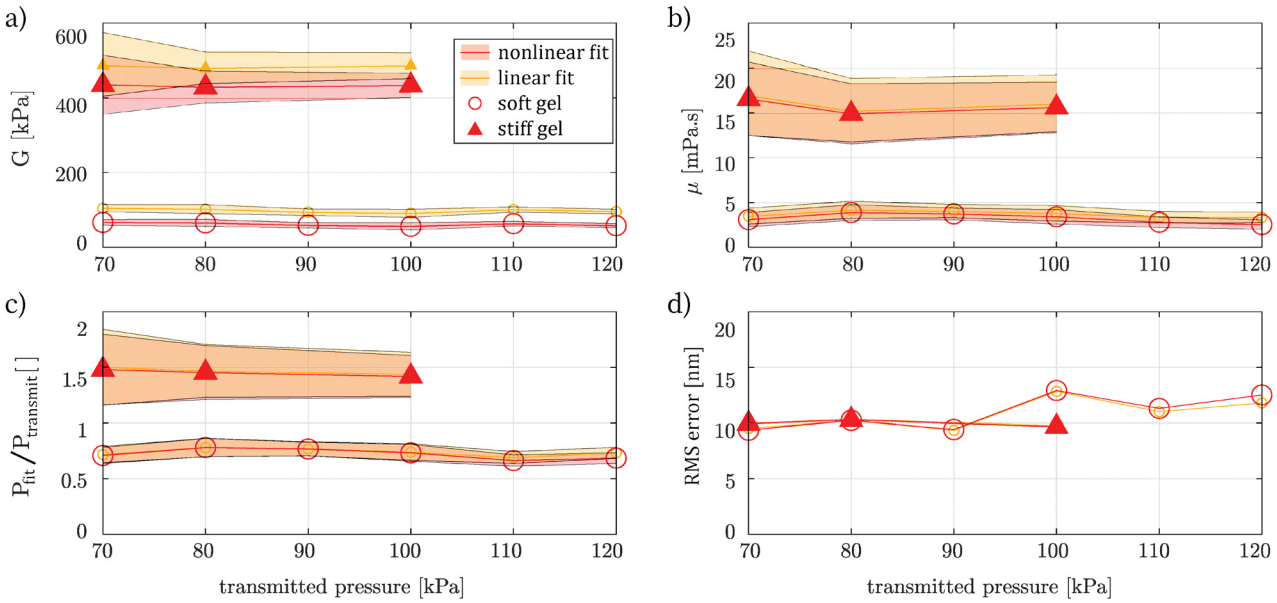

Fig. 5 (a) Fitted values of G for the soft and stiff hydrogels, and for the linear and nonlinear fits. (b) Viscosity as a function of the driving pressure. (c) Ratio of the fitted acoustic pressure to the expected acoustics pressure based on the transducer calibration performed in water. (d) Root mean square error in nanometers corresponding to the best linear and nonlinear fits. The error bars (and shadowed region) represent 95% confidence interval on the fitted parameters.

elasticity, Gaudron *et al.*[19] have demonstrated that the approximation is still valid.

The fitted values for the shear modulus G, the viscosity μ resulting from the nonlinear root mean square optimization, and the acoustic pressure P_{ac} for both hydrogels are plotted in Fig. 5a–c, respectively, as a function of the driving pressure. The error bars and shaded areas represent the 95% confidence interval for the fitted values. Fig. 5d shows the root mean square error of the best linear and nonlinear fits which are 11.0 ± 1.5 nm (mean and standard deviation) for the soft hydrogel and 10.0 ± 0.3 nm for the stiff hydrogel. Fig. 5a–c show that both linear and nonlinear fits predicts a very reproducible values across driving pressures. More specifically, for the soft hydrogel the nonlinear fit predicts a storage modulus of 61.7 ± 12 kPa while the linear fit predicts a storage modulus of 98.5 ± 14.5 kPa. Thus, while both fits feature a low residual root mean square error, these differences demonstrate the importance of using the full nonlinear equation for fitting the resonance curves. The difference between both fits in terms of viscosity is within the error margins, with μ = 3.3 ± 1.2 mPa s predicted by the nonlinear fit. For the stiff hydrogel, the nonlinear fit predicts G = 433 ± 55 kPa, against G = 484 ± 56 kPa for the linear fit, and μ = 15.7 ± 4.3. Fig. 5c shows that the ratio of the fitted acoustic pressure to the calibration pressure are 1.45 ± 0.08 and 0.72 ± 0.02. Within the confidence intervals, this ratio is constant across all applied pressures.

Since the resting radius of the bubble is extracted from diffraction-limited optical measurements, an unavoidable error in associated with its determination due to a combination of diffraction and unknown optical transfer function of the microscope objective. As we will see, this is the main confounding factor of this measurement and therefore deserves a dedicated discussion. To quantitatively evaluate the importance of R_0, we have both increased and decreased it by 5 and 10% before repeating the fitting procedure. Fig. 6 shows the result and displays the same quantities as Fig. 5 but this time as a function of the initial bubble radius. The error bars represent the standard deviation of the values across the applied acoustic pressures. The RMS error (see Fig. 6d) shows no visible influence of the initial bubble radius, suggesting that the fits are of equally good quality in all cases. The storage modulus G and the viscosity μ depend quasi-linearly on the initial radius chosen for the fit. For the soft hydrogel and the nonlinear fit, G and μ feature linear regression coefficients of 303 kPa μm^{-1} and 7.7 mPa s μm^{-1}, respectively (with adjusted coefficients of determination R^2 of 0.996 and 0.999, respectively), see Fig. 6a and b. For the stiff hydrogel, these coefficients become 787 kPa μm^{-1} and 21.5 mPa s μm^{-1} for G and μ, respectively (with adjusted coefficients of determination R^2 of 0.998 and 0.998, respectively). A ±5% error in the measurement of the initial bubble radius thus represents an error, for G and μ, of ±25 kPa and ±0.65 mPa s in the soft gel, and of ±89 kPa and ±2.4 mPa s in the stiff gel. The uncertainty in R_0 is thus larger than both the confidence intervals of the fits in the soft gel, and comparable to it in the stiff gel. The outcome of the linear fit show similar behavior, still with a larger prediction for G.

For direct comparison, hydrogels produced with the same protocol were also characterized at low shear rates (<16 s^{-1}) using a rotational rheometer. Fig. 7 provides the result for a 5% strain for the soft and stiff hydrogel. The mean values of the storage modulus are G' = 74 kPa and 144 kPa, respectively. The blue solid lines represent the expected G' behavior within a Kelvin–Voigt model. Finally, the red dashed lines represent the expected G'' for a viscosity equal to that of water which is the

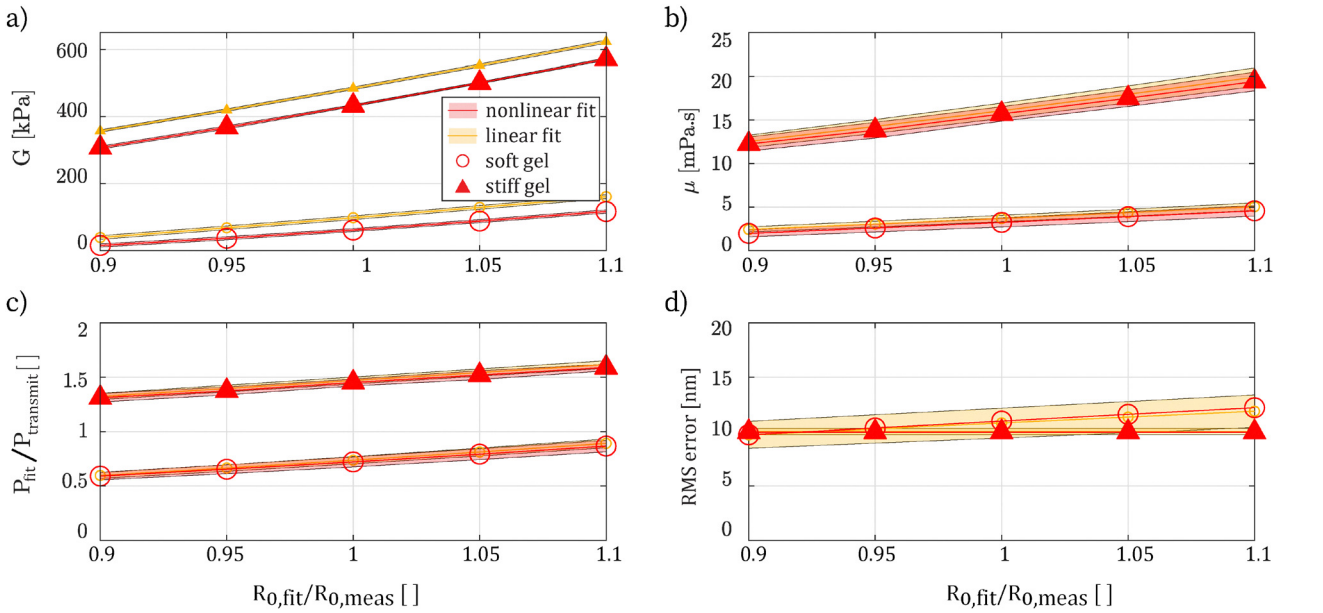

Fig. 6 (a) Fitted values of G as a function of the resting radius of the bubble used for the fit. $R_{0,\mathrm{fit}}$ is the radius used for the fitting procedure, and $R_{0,\mathrm{meas}}$ is the radius measured optically. (b) Viscosity extracted from the fit. (c) Ratio of the fitted acoustic pressure to the expected acoustics pressure based on the transducer calibration performed in water. (d) Root mean square error in nanometers corresponding to the best linear and nonlinear fits. The error bars (and shadowed region) the standard deviation of the predictions as a function of the acoustic pressure (see Fig. 5).

minimum loss modulus that can be expected for these water-based hydrogels.

Fig. 7 shows the values of G' for a strain rate on the order of $10^6\ \mathrm{s}^{-1}$ for the soft (Fig. 7a) and the stiff (Fig. 7b) hydrogels. For these specific hydrogels, these values are comparable to those obtained in the low-frequency range. The horizontal error bars of optical measurements correspond to the full width half maximum of the envelop used for the residual in the fit. The vertical error bars are the accumulated error margins, *i.e.*, the sum of the standard deviation across the different transmitted pressures, of the 95% confidence intervals, and of the uncertainty caused by a ±5% uncertainty in R_0. Interestingly, the relative uncertainty in the stiff gel is lower than in the soft gel: ±33% and ±43% for G' and G'', respectively, in the stiff gel *versus* ±62% and ±58%, respectively, in the soft gel. While G' shows little frequency dependency, $G'' = \mu\omega$ is 3 orders of magnitude larger in the MHz range than at low-strain rates. At high frequencies, G'' exhibits a behavior similar to that of water, but differs significantly from it at low frequencies.

5 Discussion and conclusion

It is important to note that, while soft tissues and associated therapies are a motivation for this proof-of-concept study and that there remains a significant gap between the simple hydrogels we use here, and soft tissues that present inhomogeneities on multiple scales, *i.e.*, from smaller than the bubble size (collagen matrix, organelles, *etc.*) to that larger than the bubble scale (cells, vessels, *etc.*). It remains to be seen to what extent tissue may be considered as a continuous medium, and the quality of the information that can be extracted from such a model. The complexity of tissue may ultimately require a statistical description within a 3D model of tissue as an inhomogeneous medium.

Underestimating R_0 will lead to an underestimation of G, since eqn (4), where $f_0 \sim \sqrt{G}/R_0$, and to an underestimation of μ since the damping (derived from eqn (3)) has the shape $\zeta \sim \kappa_s/R_0^3$. A similar observation can be made in Fig. 6. This effect is stronger than the uncertainty on the driving pressure. The initial radius R_0 is defined as the radius of the bubble measured at the start of the experiments, assuming that the system is perfectly at rest and not pre-constrained. However, the resting radius of the bubble slightly decreases during the measurement. There is thus a build-up of stress around the bubble. This stress can be expressed as an additional pressure term $P_{\mathrm{stress}} = \frac{4}{3} G \frac{R_0^3(t>0) - R_0^3(t=0)}{R_0^3(t>0)}$. For instance, in the soft hydrogel measurements, the initial radius was approximately 1.69 μm in the first measurement (P_{ac} = 70 kPa), and dropped to approximately 1.66 μm in the last measurement (P_{ac} = 120 kPa). While in principle it is easy to incorporate this factor into the simulations, it requires accurate sizing which in the present case was limited by the optical imaging system.[52]

Each bubble is exposed to 41 ultrasound pulses for each driving frequency, as shown in Fig. 3c. It is therefore possible that the composition of the bubble gas core changes over time as a result of diffusive processes, *e.g.*, that C_4F_{10} is partly replaced by air, thereby changing the polytropic exponent γ, see eqn (2). A 10% decrease in γ will yield a prediction error of about 7 kPa for G, based on eqn (4), notably from the first term. However, this potential error is less than 10%, even in the soft hydrogel.

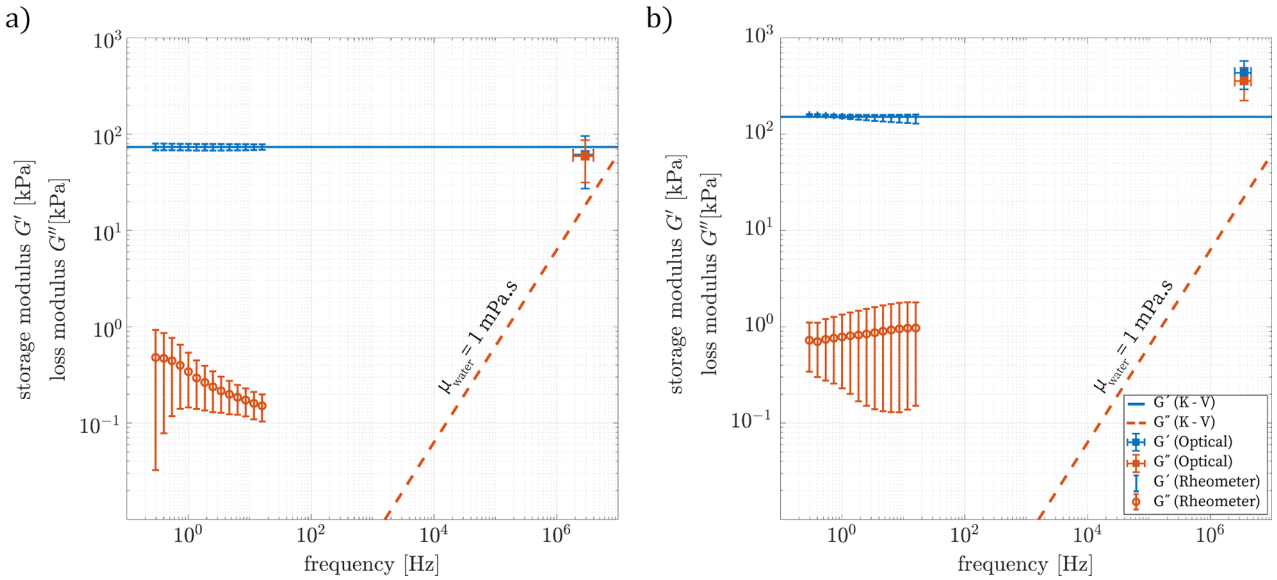

Fig. 7 A comparison between the data obtained at low strain rates ($<16\ s^{-1}$) using a rotational rheometer and at high strain rates ($>10^6\ s^{-1}$) using ultra-high-speed imaging of the microbubble oscillations for (a) the "soft" hydrogel and (b) the "stiff" hydrogel. The horizontal error bars of optical measurements correspond to the full width half maximum of the envelop used for the residual in the fit. The vertical error bars are the accumulated error margins, *i.e.*, the sum of the standard deviation across the different transmitted pressures, of the 95% confidence intervals, and of the uncertainty caused by a ±5% uncertainty in R_0.

The measurement concept proposed here makes use of the resonant response of microbubbles. The resonance is essential to be able to accurately fit the data and extract the viscoelastic parameters of the hydrogel. Thus, this method cannot be applied to viscoelastic media that feature a strongly increasing loss modulus at high strain rates, like *e.g.* PDMS, since this leads to overdamped bubble dynamics.[53] Likewise, it is not *a priori* clear whether all tissues will allow resonant oscillations in the MHz range.[23]

The study, while relying on optical methods, also opens possibilities to characterize opaque materials, such as soft tissues, where the resonance curves may be obtained through acoustic attenuation or acoustic scattering instead.[10] Our approach assumes that the viscoelastic material is homogenous on the scale of the microbubble. The microstructure of hydrogels comprises pores of the order of 1 nm[54–56] which justifies the assumption. Furthermore, our experiments show none of the symmetry breaking in the bubble dynamics that would be expected from the presence of larger pore sizes, *i.e.* of the order of the bubble size.

Using both experimental and numerical methods, we have successfully used monodisperse, phospholipid-coated microbubbles to measure the storage and loss moduli of hydrogels at MHz strain rates. While these results on simple hydrogels do not translate directly to the complex nature of real tissue, we believe these results may be relevant to the future development of methods for quantifying tissue rheology.

Conflicts of interest

There are no conflicts to declare.

Data availability

The data supporting the findings of this study are available from the corresponding author upon request.

Acknowledgements

This project has received funding from the European Union's Horizon 2020 research and innovation programme UCOM Ultrasound Cavitation in Soft Materials under the Skłodowska-Curie grant agreement no. 813766. The authors also acknowledge funding from the 4TU Precision Medicine program supported by High Tech for a Sustainable Future. G. L. also acknowledges funding from the European Union (ERC Starting Grant Super-FALCON, project number 101076844). Views and opinions expressed are however those of the author(s) only and do not necessarily reflect those of the European Union or the European Research Council Executive Agency. Neither the European Union nor the granting authority can be held responsible for them. Nathan Blanken's contribution to our paper is deeply appreciated. His thoughtful discussions and readiness to help have greatly benefited our work.

References

1 E. Stride, T. Segers, G. Lajoinie, S. Cherkaoui, T. Bettinger, M. Versluis and M. Borden, *Ultrasound Med. Biol.*, 2020, **46**, 1326–1343.
2 S. Roovers, T. Segers, G. Lajoinie, J. Deprez, M. Versluis, S. C. De Smedt and I. Lentacker, *Langmuir*, 2019, **35**, 10173–10191.

3 C. S. Lee and K. W. Leong, *Curr. Opin. Biotechnol*, 2020, **66**, 78–87.
4 K. F. Timbie, B. P. Mead and R. J. Price, *J. Controlled Release*, 2015, **219**, 61–75.
5 K. Sarkar, A. Katiyar and P. Jain, *Ultrasound Med. Biol.*, 2009, **35**, 1385–1396.
6 J. J. Kwan and M. A. Borden, *Soft Matter*, 2012, **8**, 4756–4766.
7 M. Versluis, E. Stride, G. Lajoinie, B. Dollet and T. Segers, *Ultrasound Med. Biol.*, 2020, **46**, 2117–2144.
8 S. M. van der Meer, B. Dollet, M. M. Voormolen, C. T. Chin, A. Bouakaz, N. de Jong, M. Versluis and D. Lohse, *J. Acoust. Soc. Am.*, 2007, **121**, 648–656.
9 J. Sijl, M. Overvelde, B. Dollet, V. Garbin, N. de Jong, D. Lohse and M. Versluis, *J. Acoust. Soc. Am.*, 2011, **129**, 1729–1739.
10 T. Segers, P. Kruizinga, M. P. Kok, G. Lajoinie, N. de Jong and M. Versluis, *Ultrasound Med. Biol.*, 2018, **44**, 1482–1492.
11 B. Dollet, P. Marmottant and V. Garbin, *Annu. Rev. Fluid Mech.*, 2019, **51**, 331–355.
12 P. A. Dayton, J. E. Chomas, A. F. Lum, J. S. Allen, J. R. Lindner, S. I. Simon and K. W. Ferrara, *Biophys. J.*, 2001, **80**, 1547–1556.
13 S. Qin and K. W. Ferrara, *Ultrasound Med. Biol.*, 2007, **33**, 1140–1148.
14 N. Hosseinkhah and K. Hynynen, *Phys. Med. Biol.*, 2012, **57**, 785–808.
15 C. Chen, Y. Gu, J. Tu, X. Guo and D. Zhang, *Ultrasonics*, 2016, **66**, 54–64.
16 C. F. Caskey, S. M. Stieger, S. Qin, P. A. Dayton and K. W. Ferrara, *J. Acoust. Soc. Am.*, 2007, **122**, 1191–1200.
17 A. Jamburidze, M. De Corato, A. Huerre, A. Pommella and V. Garbin, *Soft Matter*, 2017, **13**, 3946–3953.
18 E. Vlaisavljevich, K.-W. Lin, M. T. Warnez, R. Singh, L. Mancia, A. J. Putnam, E. Johnsen, C. Cain and Z. Xu, *Phys. Med. Biol.*, 2015, **60**, 2271.
19 R. Gaudron, M. Warnez and E. Johnsen, *J. Fluid Mech.*, 2015, **766**, 54–75.
20 J. S. Allen and R. A. Roy, *J. Acoust. Soc. Am.*, 2000, **107**, 3167–3178.
21 J. S. Allen and R. A. Roy, *J. Acoust. Soc. Am.*, 2000, **108**, 1640–1650.
22 E. Stride and N. Saffari, *Ultrasound Med. Biol.*, 2004, **30**, 1495–1509.
23 A. T. Oratis, K. Dijs, G. Lajoinie, M. Versluis and J. H. Snoeijer, *J. Acoust. Soc. Am.*, 2024, **155**, 1593–1605.
24 J. B. Estrada, C. Barajas, D. L. Henann, E. Johnsen and C. Franck, *J. Mech. Phys. Solids*, 2018, **112**, 291–317.
25 H. S. Fogler and J. D. Goddard, *Phys. Fluids*, 1970, **13**, 1135–1141.
26 A. Niederquell, A. C. Völker and M. Kuentz, *Int. J. Pharm.*, 2012, **426**, 144–152.
27 Z. Xing, A. Caciagli, T. Cao, I. Stoev, M. Zupkauskas, T. O'Neill, T. Wenzel, R. Lamboll, D. Liu and E. Eiser, *Proc. Natl. Acad. Sci. U. S. A.*, 2018, **115**, 8137–8142.
28 V. Bertin, Z. Zhang, R. Boisgard, C. Grauby-Heywang, E. Raphaël, T. Salez and A. Maali, *Phys. Rev. Res.*, 2021, **3**, L0–32007.
29 K. Murakami, Y. Yamakawa, J. Zhao, E. Johnsen and K. Ando, *J. Fluid Mech.*, 2021, **924**, A38.
30 T. Deffieux, G. Montaldo, M. Tanter and M. Fink, *IEEE Trans. Med. Imaging*, 2008, **28**, 313–322.
31 K. Nightingale, *Curr. Med. Imaging Rev.*, 2011, **7**, 328–339.
32 H. Koruk, A. El Ghamrawy, A. N. Pouliopoulos and J. J. Choi, *Appl. Phys. Lett.*, 2015, **107**, 223701.
33 S. Catheline, J.-L. Gennisson, G. Delon, M. Fink, R. Sinkus, S. Abouelkaram and J. Culioli, *J. Acoust. Soc. Am.*, 2004, **116**, 3734–3741.
34 A. Prosperetti, *Phys. Fluids*, 1982, **25**, 409–410.
35 T. Leighton, *The Acoustic Bubble*, Academic Press, 2012.
36 T. Leighton, *Ultrasonics*, 2008, **48**, 85–90.
37 A. Prosperetti, L. A. Crum and K. W. Commander, *J. Acoust. Soc. Am.*, 1988, **83**, 502–514.
38 P. Marmottant, S. van der Meer, M. Emmer, M. Versluis, N. de Jong, S. Hilgenfeldt and D. Lohse, *J. Acoust. Soc. Am.*, 2005, **118**, 3499–3505.
39 T. Segers, E. Gaud, M. Versluis and P. Frinking, *Soft Matter*, 2018, **14**, 9550–9561.
40 E. Brujan, *Cavitation in Non-Newtonian Fluids: With Biomedical and Bioengineering Applications*, Springer Berlin Heidelberg, 2011.
41 H. Barnes, I. of Non-Newtonian and F. Mechanics, *A Handbook of Elementary Rheology*, University of Wales, Institute of Non-Newtonian Fluid Mechanics, 2000.
42 C. Devin Jr, *J. Acoust. Soc. Am.*, 1959, **31**, 1654–1667.
43 J. Sijl, B. Dollet, M. Overvelde, V. Garbin, T. Rozendal, N. de Jong, D. Lohse and M. Versluis, *J. Acoust. Soc. Am.*, 2010, **128**, 3239–3252.
44 J. Liu, H. Zheng, P. S. Poh, H.-G. Machens and A. F. Schilling, *Int. J. Mol. Sci.*, 2015, **16**, 15997–16016.
45 P. A. Janmey and R. T. Miller, *J. Cell Sci.*, 2011, **124**, 9–18.
46 B. Van Elburg, G. Collado-Lara, G.-W. Bruggert, T. Segers, M. Versluis and G. Lajoinie, *Rev. Sci. Instrum.*, 2021, **92**, 035110.
47 T. Segers, L. de Rond, N. de Jong, M. Borden and M. Versluis, *Langmuir*, 2016, **32**, 3937–3944.
48 T. Segers, E. Gaud, G. Casqueiro, A. Lassus, M. Versluis and P. Frinking, *Appl. Phys. Lett.*, 2020, **116**, 173701.
49 A. S. Mikhail, A. H. Negussie, C. Graham, M. Mathew, B. J. Wood and A. Partanen, *Med. Phys.*, 2016, **43**, 4304–4311.
50 A. H. Negussie, A. Partanen, A. S. Mikhail, S. Xu, N. Abi-Jaoudeh, S. Maruvada and B. J. Wood, *Int. J. Hyperthermia*, 2016, **32**, 239–243.
51 G. Lajoinie, Y. Luan, E. Gelderblom, B. Dollet, F. Mastik, H. Dewitte, I. Lentacker, N. de Jong and M. Versluis, *Commun. Phys.*, 2018, **1**, 22.
52 C. A. Sennoga, J. S. Yeh, J. Alter, E. Stride, P. Nihoyannopoulos, J. M. Seddon, D. O. Haskard, J. V. Hajnal, M.-X. Tang and R. J. Eckersley, *Ultrasound Med. Biol.*, 2012, **38**, 834–845.
53 M. Bruning, M. Costalonga, J. Snoeijer and A. Marin, *Phys. Rev. Lett.*, 2019, **123**, 214501.
54 M. Kremer, E. Pothmann, T. Roessler, J. Baker, A. Yee, H. Blanch and J. M. Prausnitz, *Macromolecules*, 1994, **27**, 2965–2973.
55 L. M. Lira, K. A. Martins and S. I. Córdoba de Torresi, *Eur. Polym. J.*, 2009, **45**, 1232–1238.
56 N. L. Cuccia, S. Pothineni, B. Wu, J. Méndez Harper and J. C. Burton, *Proc. Natl. Acad. Sci. U. S. A.*, 2020, **117**, 11247–11256.

